Dynamic structural response and deformations of monolayer MoS_2 visualized by femtosecond electron diffraction

Ehren M. Mannebach[1], Renkai Li[2], Karel-Alexander Duerloo[1], Clara Nyby[3], Peter Zalden[4], Theodore Vecchione[2], Friederike Ernst[4,5,6], Alexander Hume Reid[4], Tyler Chase[4,5], Xiaozhe Shen[2], Stephen Weathersby[2], Carsten Hast[2], Robert Hettel[2], Ryan Coffee[2], Nick Hartmann[2], Alan R. Fry[2], Yifei Yu[7], Linyou Cao[7], Tony F. Heinz[4,5,6], Evan J. Reed[1,7], Hermann A. Dürr[4], Xijie Wang[2], Aaron M. Lindenberg[1,4,6]∗*

[1]Department of Materials Science and Engineering, Stanford University, Stanford, CA 94305

[2]SLAC National Accelerator Laboratory, Menlo Park, CA 94025

[3]Department of Chemistry, Stanford University, Stanford, CA 94305

[4]Stanford Institute for Materials and Energy Sciences, SLAC National Accelerator Laboratory, Menlo Park, CA 94025

[5]Department of Applied Physics, Stanford University, Stanford, CA 94305

[6]PULSE Institute, SLAC National Accelerator Laboratory, Menlo Park, CA 94025

[7]Department of Materials Science and Engineering, North Carolina State University, Raleigh, North Carolina, 27695

*Address correspondence to aaronl@stanford.edu

Supplementary Information

1. Time Response of All {0001} Zone Axis Diffraction Peaks

Fig. S1 shows the time response of the diffraction intensity for all five diffraction peak families shown in Fig. 1a. As stated in the main text, the time scale of the initial diffraction intensity decrease (Fig. S1a) reflects the electron-phonon coupling time, while the longer time scales in Fig. S1b correspond to the MoS_2 monolayer thermally equilibrating with its environment.

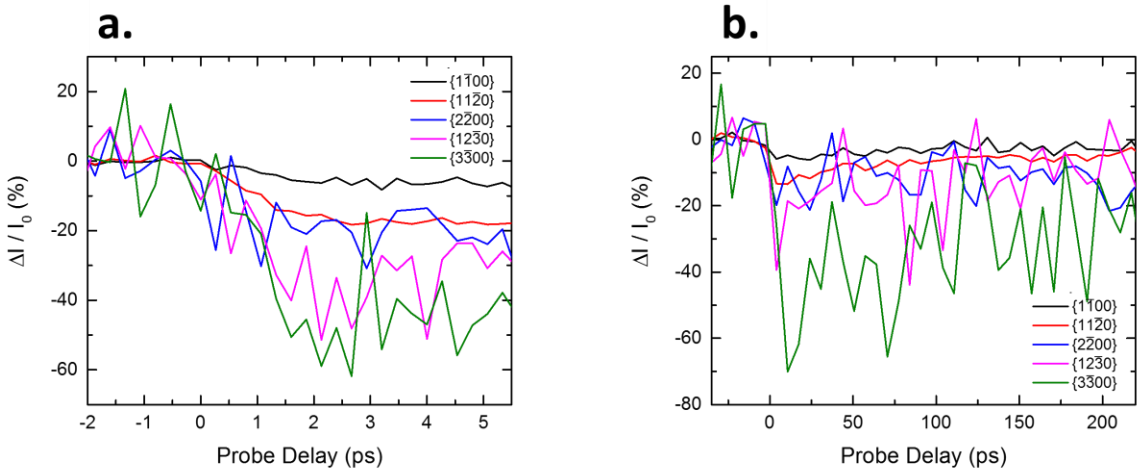

Figure S1: Time response of the diffraction intensity with incident pump fluence ~ 3.3 mJ/cm^2.

2. Calculation of the Structure Factor from Molecular Dynamics Simulations

The structure factors shown in Figure 3a of the main text are used to compare simulation data with experimental data and were directly calculated using atomic positions from the molecular dynamics simulations detailed elsewhere in this paper. The structure factor is given by $F(\vec{Q}) = \sum_i f_i^B(\vec{Q}) \cdot e^{-i\vec{Q}\cdot\vec{R_i}}$, where f_i^B is the atomic scattering factor for electrons for atom *i*, $\vec{Q}$ is the electron scattering vector for the *(hkl)* peak, and $\vec{R_i}$ is the position of atom *i*. If we take $\vec{R} = r_x\vec{a_1} +$

$r_y\overrightarrow{a_2} + r_z\overrightarrow{a_3}$ and $\vec{Q} = h\overrightarrow{a_1^*} + k\overrightarrow{a_2^*} + l\overrightarrow{a_3^*}$ and recognize that $\overrightarrow{a_i} \cdot \overrightarrow{a_j^*} = 2\pi\delta_{ij}$, where δ_{ij} is the Kronecker delta function, $\vec{Q} \cdot \vec{R}$ becomes $2\pi(hr_x + kr_y + lr_z)$. The structure factor can then be written as $F_{hkl} = \sum_i f_i^B(Q_{hkl}) \cdot e^{-2\pi i(hr_x+kr_y+lr_z)}$, where *h*, *k*, and *l* are the Miller indices of the atomic planes. (Please note that in the main text we use the Miller-Bravais indices *(hkil)* as opposed to the *(hkl)* Miller indices of this calculation, where the index *i* is given by *–(h+k)*. The addition of this fourth index makes permutation symmetries within a peak family apparent for hexagonal lattice systems.) The atomic scattering factors for electrons were put in terms of that for x-rays using the Mott-Bethe formula, $f^B(Q,Z) = \frac{me^2}{2\pi\hbar^2\varepsilon_0}\left\{\frac{Z-f(Q,Z)}{Q^2}\right\}$, where *f* is the atomic scattering factor for x-rays, and Z is the atomic number. Values for $f(Q,Z)$ were calculated using analytical fits from Su and Coppens.[1]

3. Pump-Induced Thermal Effects in MoS_2 on Amorphous Carbon

3.1 Estimation of temperature jump from known optical and thermal properties

The temperature jumps in the MoS_2 monolayer and underlying amorphous carbon substrate can be estimated from the known absorbance and heat capacity for each material. Assuming perfect flatness of the layers and interfaces, using the permittivities at 400 nm of $\varepsilon_{MoS_2} = 3.8 + 32i$[2] and $\varepsilon_{a-C} = 5.5 + 4.3i$,[3] we calculate 29.1% of the incident pump energy is reflected, and 29.9% is transmitted. The remaining energy is absorbed by the MoS_2/*a*-C stack: 6.6% of the total incident light in the MoS_2 and 33.0% in the *a*-C. With an incident pump pulse energy of 30 μJ over a pump area of ~0.9 mm^2, the MoS_2 and *a*-C layers absorb 2.0 μJ and 9.9 μJ, respectively. Using the specific heat values from Table S1, we estimate temperature jumps of 1900 K in the MoS_2 and 220 K in the *a*-C. These simple estimates ignore any surface roughness/imperfections in the MoS_2/*a*-

C stack, temperature-dependent changes in thermal properties, and saturable absorption effects,[4] all of which would cause an over-estimate in the amount of absorbed pump energy and induced temperature jump.

Table S1: Parameters used in the COMSOL simulation.

	Density (kg m^{-3})	**Specific Heat (J kg^{-1} K^{-1})**	**Thermal conductivity (W m^{-1} K^{-1})**
MoS_2[5]	5060	373.5	34.5
a-C[6,7]	1900	1300	1
Cu	8700	385	400

3.2 Heat flow simulations

COMSOL simulations were performed to model the thermal transport dynamics in the MoS_2/*a*-C/Cu system of the MoS_2/TEM grid samples. In the simulation, the sample is assumed to have full rotational symmetry around an axis perpendicular to the center of the membrane. The membrane then has an approximate free-standing diameter of 35 μm, after which it is assumed to be in contact with a 10 μm high and 10 μm radius copper ring. The thickness of the MoS_2 monolayer and *a*-C substrate are taken as 0.6 nm and 20 nm, respectively. The incoming pump fluence is further assumed to be constant (homogeneous) over the 90 μm diameter of the sample, and we assume that the entire pump energy is transformed to lattice heat before thermal transport begins. A schematic of the geometry of this simulation in shown in Figure S2. Table S1 gives the remaining parameters used in the simulation. The heat flow is simulated according to $\rho C_p \frac{\partial T}{\partial t} = \vec{\nabla} \cdot \left(k \vec{\nabla} T\right)$, where ρ is the density, k is the thermal conductivity, and C_p is the specific

heat. An additional thermal boundary resistance is included between the films to simulate the interface between the MoS_2 and the *a*-C. This resistance is modeled by

$$\vec{n}_t\left(-k_t\vec{\nabla}T_t\right) = \frac{T_b - T_t}{R_s}$$

$$\vec{n}_b\left(-k_b\vec{\nabla}T_b\right) = \frac{T_t - T_b}{R_s}$$

Here, R_s is the thermal boundary resistance, T_t and T_b are the top and bottom temperatures over the interface, and $\vec{n}$ is the normal vector to the respective interface. A thermal boundary conductance of 15 MW m^{-2} K^{-1} matches the simulation timescales to those of the experiment. Figure S3 shows how the heat from the MoS_2 flows into the *a*-C flows over ~75 ps. The diffusion of heat out of the MoS_2/*a*-C membrane into the rest of the TEM grid takes ~100 µs, consistent with full recovery from pulse to pulse at the 120 Hz repetition rate of the experiment.

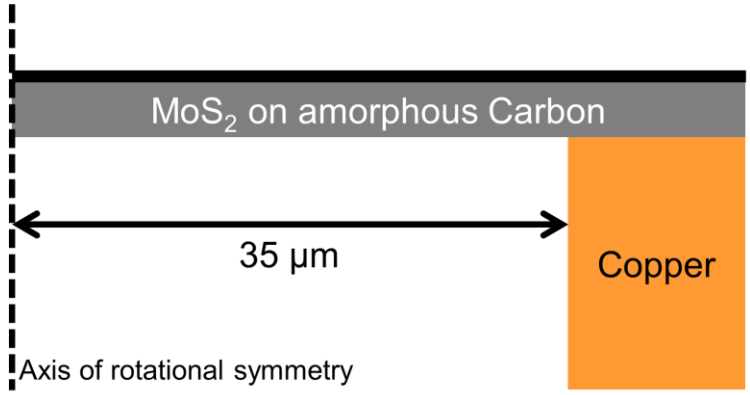

Figure S2: Schematic of the COMSOL simulation geometry.

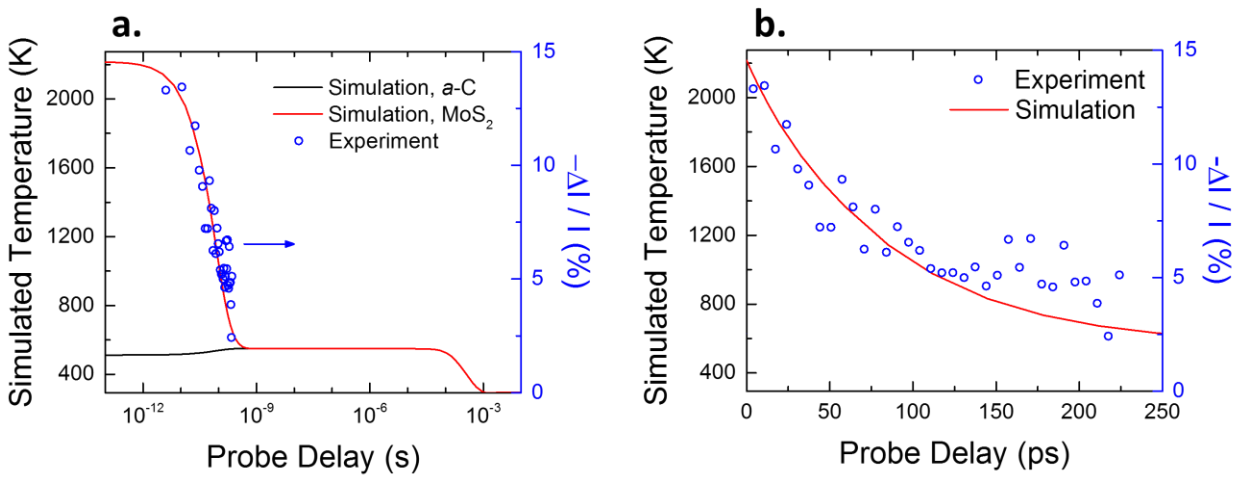

Figure S3: Overlay of experimental data on COMSOL simulations showing thermal transport in the MoS2/TEM grid system with probe delay time on a log scale (a) and a linear scale (b).

3.3 Debye-Waller factor simulations

The electron diffraction pattern of monolayer MoS_2 has been calculated using a 3 nm-diameter supercell (Figure S4a) of the primitive MoS_2 unit cell using

$$I(\vec{Q}) \propto \sum_j \left(\frac{Z_j - f_j^x(Q)}{Q^2}\right) \cdot \exp\left(-\langle u_j^2\rangle Q^2\right) \cdot \exp\left(-i2\pi\vec{Q}\cdot\vec{r_j}\right)$$

Here, Z is the atomic number, f^x is the atomic scattering factor for x-rays, $\vec{r_j}$ is the position of atom j in the supercell, and $\langle u_j^2\rangle$ is the mean square displacement for atom j. By summing over all atoms in the supercell, we can simulate a diffraction pattern (Figure S4b). $\langle u_j^2\rangle$ can be calculated for any temperature using

$$\langle u_j^2\rangle = \frac{3\hbar^2}{2m_j k_B \theta_D} \cdot \left(\frac{1}{4} + \frac{T}{\theta_D}\right) \cdot \frac{2}{3}$$

where m_j is the atomic mass of atom j and θ_D is the Debye temperature (θ_D = 580 K for bulk MoS_2).[8] The additional factor of ⅔ comes in because the diffracted intensity in this experiment is

only sensitive to in-plane vibrations, *i.e.* $\langle u_j^2 \rangle$ contains only two of the three degrees of freedom in the crystal.

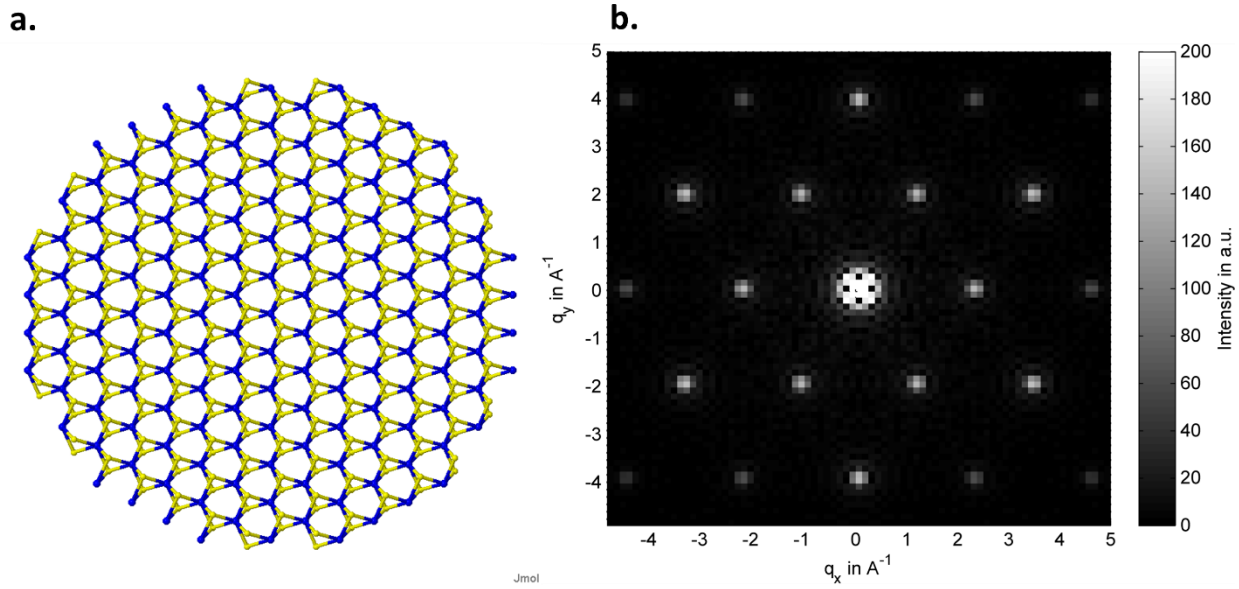

Figure S4: (a) Supercell used in the calculation of diffraction intensity as a function of temperature. (b) Simulated diffraction pattern of MoS2 monolayer at 300 K.

Using the equations above, we can calculate the temperature dependence of the scattering intensity for each diffraction peak studied in the experiment. Figure S5 shows this temperature dependence for the $\{11\bar{2}0\}$ reflection. Similar to the approach of comparing the structure factors of an elevated and room temperature MD simulation frame to the diffraction intensity modulation seen in the experiment, we find a temperature jump of ~1760 K in this Debye-Waller simulation matches the experimental results. This estimation is in good agreement with the temperature jump calculated in Section 3.1 of this Supplementary Information.

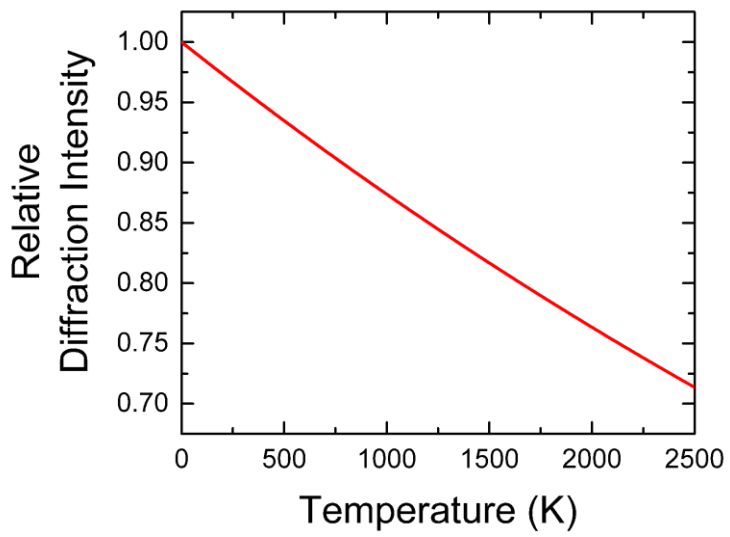

Figure S5: Scaling of diffraction intensity with temperature for the {11-20} peak, as calculated using the Debye-Waller analysis.

4. Calculation of Ripple Angle from Diffraction Peak Broadening

As shown in Figure 5(c–d) of the main text, rippling of a two-dimensional material creates a distribution of diffracted intensity in cone-shaped regions of reciprocal space. This distribution manifests as an increase in the width of the measured diffraction spots and can only be measured if the Ewald sphere is slightly tilted in reciprocal space by an angle φ. If we know φ, we can estimate the increase in diffraction cone angle $\Delta\theta$, which is directly proportional to the angle of the sample's local surface normal deviation by $\Delta\theta = \frac{\Delta\sigma}{Q_z} = \frac{\Delta\sigma}{\varphi(Q_{xy}-\sigma_0)}$. Since $\sigma_0 \ll Q_{xy}$, this equation simplifies to:

$$\Delta\theta = \frac{\Delta\sigma}{\varphi Q_{xy}}$$

Here Q_{xy} is the in-plane component of the momentum transfer. It should be pointed out that $\Delta\sigma$ above is obtained by subtracting in quadrature the intrinsic peak width from the measured peak width.

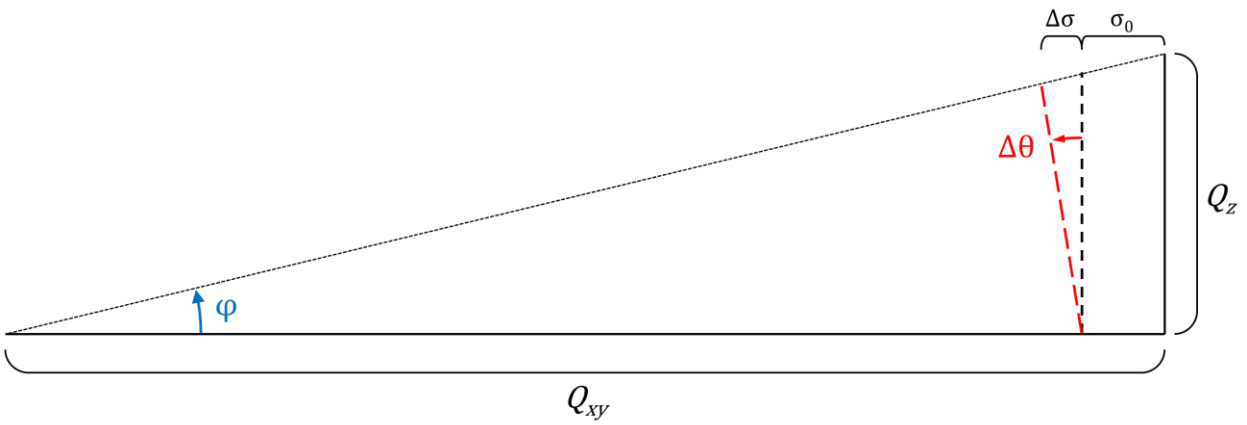

Figure S6: Schematic of how sample rippling induces peak broadening in reciprocal space. The thin dotted line represents the tilted Ewald sphere, the solid line on the right represents the center of the diffraction rod for a given reflection at Q_{xy}, the dashed black line represents the intrinsic width of the diffraction spot σ_0 due to beam divergence and other experimental imperfections, and the dashed red line represents the pump-induced cone-shaped region of reciprocal space.

5. Details of the Experimental Methods

5.1 Monolayer synthesis

Large-area, single layers of MoS_2 were grown *via* chemical vapor deposition in a tube furnace (Lindberg/Blue M™ 1100°C Tube Furnaces) with a modified growth method.[9] An Al_2O_3 crucible with sulfur powder was loaded at the upstream and MoO_3 source material was placed on a Si substrate at the center of the furnace. Several sapphire substrates were placed at the downstream

in the quartz tube. The temperature was ramped to 550 °C in 30 min, then gradually increased to 750 °C in 40 min and kept for 10 min. The whole process was under an atmosphere of Ar gas with a flux rate of 100 sccm. After growth, the system was cooled down to room temperature naturally.

5.2 Transfer process

In a typical transfer process,[10] 9 g of polystyrene (PS) with a molecular weight of 280,000 g/mol was dissolved in 100 mL of toluene, followed by spin-coating (3500 rpm for 60 s) on the target substrates. Spin-coated films were then baked at 80−90 °C for 15 min. A water droplet was then placed on top of the sample. To facilitate the penetration of water molecules, we poked the PS layer with a blade from the edge. Once the PS layer was scratched from the edge, water molecules could penetrate through all the way under MoS_2, resulting in the delamination of the PS-MoS_2 assembly. The PS-MoS_2 assembly was then be picked up with tweezers and transferred to a TEM grid (Ted Pella-Quantifoil). To ensure the uniformity of the transferred MoS_2, we baked the transferred PS-MoS_2 assembly at 80 °C for 1 h and performed a final baking for 30 min at 150 °C. Finally, the PS was removed by rinsing with toluene several times. Samples were characterized by both Raman and optical microscopy prior to the experiments.

5.3 Experiment

Measurements are carried out using 2.1 MeV kinetic energy electron beams generated at the ASTA ultrafast electron diffraction (UED) system at the SLAC National Accelerator Laboratory. The ASTA MeV UED consists of an S-band photocathode RF gun, RF synchronized laser system, electron beam diagnostic and collimation system, sample chamber and phosphor based single electron diffraction detector. Both the pump laser and probe electron beams are operated at 120

Hz repetition rate. Each electron pulse contains 9.4×10^4 electrons (15 fC) and has a 360 fs FWHM pulse duration and 350 um diameter probe size at the sample. The upper limit of the time-of-arrival jitter between the pump and probe pulses is estimated to be 110 fs FWHM using measured RF and laser timing jitter and RF stability. The temporal resolution for the reported measurement is below 400 fs FWHM.

The photocathode trigger and the trigger to the sample was generated by a 50-fs Ti:sapphire laser with a 120 Hz repetition rate and fundamental wavelength of 800 nm (1.55 eV). Optical pumping at 400 nm (3.10 eV) was achieved by frequency-doubling a split-off portion of the laser beam in a non-linear crystal (BBO). This was focused to a ~700 μm spot size on the sample. The ultrashort electron pulse was generated by frequency-tripling the remaining laser light in two non-linear crystals to generate 266 nm excitation pulses to the electron photocathode. These electrons were then focused and collimated into a beam incident on our sample. Diffracted electrons illuminated a phosphor screen that was imaged by an Andor CCD camera. Each time points corresponds to the average of ~1000 shots. Bandpass filters were used to block any residual pump light from illuminating the CCD camera. Pump and probe are collinear with visible pump beam focused to ~700 μm and electron probe focused to ~350 μm. Split-off pulses from the same regenerative amplifier generate pump and probe, thereby minimizing temporal jitter between the optical and electron beams.

5.4 Molecular dynamics simulations

Molecular Dynamics (MD) calculations were performed using density functional theory within the Projector-Augmented Wave (PAW) pseudopotential implementation of the Vienna Ab Initio

Simulation Package (VASP).[11] Electron exchange and correlation effects are described by the generalized gradient approximation (GGA) functional of Perdew, Burke and Ernzerhof.[12] We use the Γ-point implementation of VASP with automatic real-space projector operators. Wave functions are expanded in a plane-wave basis set with a cutoff of 350 eV. Orbital occupancy numbers are at their ground state values. The computational cell is an 8×8×1 hexagonal supercell (192 atoms) with a primitive lattice constant of 3.18 Å. The DFT computational cell has periodic boundary conditions and a 12.3 Å cell height in the out-of-plane direction. The initial positions in the MD calculations are extracted from a preliminary ionic relaxation with convergence threshold 10^{-5} eV (electronic threshold 10^{-6} eV). Using a Nosé-Hoover thermostat, we increase the target temperature from 30 K to 1070 K in 725 time steps, where each step has a duration of 5 fs. The SMASS parameter of the thermostat is set to 10^{-2}. The threshold for electronic convergence at each MD time step is 10^{-3} eV.

References

(1) Su, Z.; Coppens, P. *Acta Crystallogr. Sect. A Found. Crystallogr.* **1997**, *53* (6), 749–762.

(2) Li, Y.; Chernikov, A.; Zhang, X.; Rigosi, A.; Hill, H. M.; van der Zande, A. M.; Chenet, D. a.; Shih, E.-M.; Hone, J.; Heinz, T. F. *Phys. Rev. B* **2014**, *90* (20), 1–6.

(3) Dayana, K.; Fadzilah, a. N.; Rusop, M. *Proc. - 2011 IEEE Student Conf. Res. Dev. SCOReD 2011* **2011**, No. Di, 25–29.

(4) Mannebach, E. M.; Duerloo, K.-A. N.; Pellouchoud, L. A.; Sher, M.-J.; Nah, S.; Kuo, Y.; Yu, Y.; Marshall, A. F.; Cao, L.; Reed, E. J.; Lindenberg, A. M. *ACS Nano* **2014**, *8* (10), 10734–10742.

(5) Yan, R.; Simpson, J. R.; Bertolazzi, S.; Brivio, J.; Watson, M.; Wu, X.; Kis, A.; Luo, T.; Hight Walker, A. R.; Xing, H. G. *ACS Nano* **2014**, *8* (1), 986–993.

(6) Bullen, A. J.; O'Hara, K. E.; Cahill, D. G.; Monteiro, O.; von Keudell, A. **2000**, 4.

(7) Wiener, M.; Reichenauer, G.; Hemberger, F.; Ebert, H. P. *Int. J. Thermophys.* **2006**, *27* (6), 1826–1843.

(8) Wakabayashi, N.; Smith, H. G.; Nicklow, R. M. *Phys. Rev. B* **1975**, *12* (2), 659–663.

(9) Lee, Y.-H.; Zhang, X.-Q.; Zhang, W.; Chang, M.-T.; Lin, C.-T.; Chang, K.-D.; Yu, Y.-C.; Wang, J. T.-W.; Chang, C.-S.; Li, L.-J.; Lin, T.-W. *Adv. Mater.* **2012**, *24* (17), 2320–2325.

(10) Gurarslan, A.; Yu, Y.; Su, L.; Yu, Y.; Suarez, F.; Yao, S.; Zhu, Y. *ACS Nano* **2014**, *8* (11), 11522–11528.

(11) Kresse, G. *Phys. Rev. B* **1999**, *59* (3), 1758–1775.

(12) Perdew, J. P.; Burke, K.; Ernzerhof, M. *Phys. Rev. Lett.* **1996**, *77* (18), 3865–3868.